ACS APPLIED NANO MATERIALS

www.acsanm.org Article

Atomic Hydrogen Annealing of Graphene on InAs Surfaces and Nanowires: Interface and Morphology Control for Optoelectronics and Quantum Technologies

S. Fatemeh Mousavi, Yen-Po Liu, Giulio D'Acunto, Andrea Troian, José M. Caridad, Yuran Niu, Lin Zhu, Asmita Jash, Vidar Flodgren, Sebastian Lehmann, Kimberly A. Dick, Alexei Zakharov, Rainer Timm, and Anders Mikkelsen*

Cite This: *ACS Appl. Nano Mater.* 2022, 5, 17919−17927 Read Online

ACCESS | Metrics & More | Article Recommendations | Supporting Information

ABSTRACT: Folding two-dimensional graphene around one-dimensional III−V nanowires yields a new class of hybrid nanomaterials combining their excellent complementary properties. However, important for high-quality electrical and optical performance, needed in many applications, are well-controlled oxide-free interfaces and a tight folding morphology. To improve the interface chemistry between the graphene and InAs, we annealed the samples in atomic hydrogen. Using surface-sensitive imaging, we found that the III−V native oxides in the interface can be reduced at temperatures that maintain the graphene and the III−V nanostructures. Transferring both single- and multilayer graphene flakes onto InAs NWs, we found that single layers fold tightly around the NWs, while the multilayers fold weakly with a decline of only a few degrees. Annealing in atomic hydrogen further tightens the folding. Together, this indicates that high-quality morphological and chemical control of this hybrid material system is possible, opening for future devices for quantum technologies and optoelectronics.

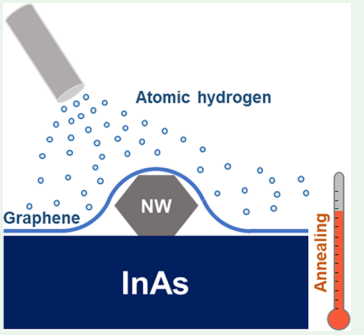

KEYWORDS: *graphene, InAs, nanowires, semiconductors, oxide, hydrogen, AFM, XPS, LEEM, XPEEM*

INTRODUCTION

Hybrid nanostructures are of significant current interest as they combine high-performance features of several individual nanostructures into systems with more complete sets of excellent properties.[1] Metallic graphene and semiconducting III−V compound NWs are two classes of nanomaterials with very different properties. The inertness,[2] extreme conductivity,[3−5] optical transparency,[6−9] and mechanical flexibility[10−13] of the graphene have made it a good candidate to be widely used as a potential high-performance electrode[7−9] and protective layer.[14,15] This can be combined with the excellent optical and transport properties of the III−V semiconductors,[16,17] with promises for optoelectronic and photovoltaic[18] as well as quantum technology applications.[16,17] Combining graphene with semiconductor NWs has been resulted in a wide range of interesting applications, such as transparent organic single crystal field-effect transistors,[7] NW devices with graphene electrodes,[8,19−21] high-responsivity graphene/InAs NW heterojunction photodetectors,[22] graphene-coated waveguides,[23] and photonic integrated sources.[24] To realize the full performance potential for these and many other applications, both morphology and graphene/semiconductor interface must be controlled. Defect-free interfaces are important to realize transport properties, enabling graphene plasmonics, quantum technologies,[25] and high optical efficiencies of these systems.[26−28] The ability of graphene to fold tightly over nanostructures is important to create good contacts, for protection and wrap-around gating.[29,30]

Removal of the native oxide is an important point to achieve well-functioning semiconductor devices. Oxides can hinder the formation of ohmic contacts, and defects in the oxides can be detrimental to transport and optical properties. For III−V semiconductor NWs, this has been shown in many studies.[31−37] Annealing semiconductor surfaces in atomic hydrogen has been proven to be efficient in removing native oxides and achieving clean, defect-free surfaces.[38] This in turn leads to improved properties of the NWs.[31,32,37,39] The hydrogen radicals will react with the oxide and other contaminants on the surface to form more volatile compounds, which desorb below the temperature where the samples decompose.[40,41] However, graphene can act as a barrier for diffusion to and from the underlying substrate that can lead to an inhibition of the deoxidation processes.[42−45] Furthermore,

Received: September 2, 2022
Accepted: November 2, 2022
Published: November 22, 2022

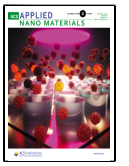

passivation of dangling bonds at the interface between graphene and SiC[46] was impeded at temperatures up to ∼800 °C, and as a result, the sample underneath the graphene could not be passivated. Therefore, the potential of atomic hydrogen cleaning underneath graphene is a nontrivial question with relevance for applications using the systems' electronic or optical properties.

In the present work, we place the graphene flakes with varying number of layers on top of InAs surfaces with Au lithographic patterns and deposited InAs NWs. The placement of graphene on both flat surfaces, NWs and metal pattern, can be confirmed using optical and electron microscopy. The number of graphene layers is determined using Raman spectroscopy. Using atomic force microscopy (AFM), we found that while single layers fold tightly around the NWs, multilayers are stiffer and, thus, only fold weakly with a linear slope of a few degrees. By treating samples with atomic hydrogen at 400 °C, it is possible to reduce the III−V native oxides also underneath the graphene. This is confirmed using low-energy electron microscopy (LEEM), synchrotron-based micro-X-ray photoelectron spectroscopy (μXPS), and X-ray photoemission electron microscopy (XPEEM). These techniques map out the surface chemistry and morphology with nanometer resolution. We found that the treatment leaves the graphene and the NWs intact. Furthermore, AFM measurements indicate that the treatment will lead to a tighter folding of even multilayer graphene around the NWs.

METHODS AND MATERIALS

Hydrogen Cleaning. The InAs samples were cleaned using hydrogen cracker (MBE-Komponenten HABS). To remove the native oxide and other impurities, atomic hydrogen cleaning has been efficient for InAs substrate and NW surfaces. Thus, samples can be introduced to a UHV chamber and native oxides removed using hydrogen cleaning.[32,47,48] Hydrogen gas was introduced into the preparation chamber through a leak valve ($P \sim 5 \times 10^{-6}$ mbar) and thermally cracked at around 1700 °C to atomic hydrogen (H*).[49] Samples were annealed at 400 °C in parallel for full cleaning and to remove hydrocarbons and oxides.

Synthesis of the Nanowires. InAs NWs with two engineered segments consisting of either wurtzite or zinc blende were prepared by low pressure metal organic vapor phase epitaxy (MOVPE) on epiready InAs <111>B substrates (Figure S1). Trimethylindium (TMIn) and arsine (AsH_3) were used as precursors and Au aerosol particles[50] with a nominal diameter of 30 nm served as seed for the vapor−liquid−solid (VLS) growth[51] of the nanowires. A close coupled showerhead AIXTRON 3 × 2″ system (CCS) was operated at a pressure of 100 mbar and a total carrier gas flow of 8 slm. The growth process was initiated by annealing the aerosol-covered growth substrate for 10 min in an AsH_3/H_2 environment at a set temperature of 550 °C with an AsH_3 molar fraction of $\chi_{AsH_3} = 2.5 \times 10^{-3}$. After setting a growth temperature of 470 °C, first the wurtzite and then zinc blende segments were grown at respective molar fractions of $\chi_{TMIn} = 1.8 \times 10^{-6}$ and of $\chi_{AsH_3} = 1.3 \times 10^{-4}$, 2.3×10^{-5}, and -2.5×10^{-2} with growth times of about 15 min, respectively. NW growth was finished by a 40-s wurtzite growth step before being terminated by cutting the TMIn supply and cooling under the same AsH_3/H_2 ambience as used for the annealing down to a set temperature of 300 °C.

Atomic Force Microscopy. In-air AFM was performed using a JPK AFM in tapping mode, whose cantilever tip is made of silicon with Pt/Ir coating. The resonant frequency of the standard Si cantilever is around 300 kHz. The scanning parameters are 50 and 1 for I and P gain, respectively.

LEEM, XPEEM, and μXPS. LEEM and XPEEM measurements were conducted at the MAXPEEM beamline of MAX IV Laboratory, Sweden. The beamline is a typical soft X-ray beamline with an energy range from 30 to 1500 eV. The energy resolution, $E/\Delta E$, was estimated to be >2000, and the flux is up to 1013 photon/s by utilizing a modified SX-700 monochromator with a 300 line/mm grating. The microscope used is an aberration corrected spectroscopic photoemission and low-energy electron microscope (AC-SPELEEM) from Elmitec GmbH, Germany. The microscope can work at varied operation modes, i.e., LEED, LEEM, (X)PEEM, XPS, and ARPES. In a complementary way, these modes provide the morphologic, chemical, electronic, and structural information of the sample from both real and momentum spaces. In LEEM mode, the image is formed by the elastic reflected/scattered electrons from the sample surface that was illuminated with a collimated electron beam at low energy (<1000 eV). While the energy of the electrons is less than or equal to zero, the electrons are reflected 100% and a so-called mirror electron microscopy (MEM) image is formed. MEM is normally used to map the difference of work function or morphology on the sample. In this study, the core-level XPEEM images were taken with an energy window ΔE = ∼0.5 eV. The image directly presents the element mapping at the selected core-level across the sample area illuminated by the photon beam (∼20 μm). In AC-SPELEEM, μXPS, similar to the conventional XPS, can be acquired from a small area down to 1 μm by using a select area aperture. In this mode, the photoelectrons are projected proportional to their kinetic energies along a narrow line on the dispersive plane of the microscope's energy analyzer. This line's profile can be easily converted into an expression of photoelectron intensity versus binding energy as used in the conventional XPS. This method provides better energy resolution compared with the core-level XPEEM imaging that has better spatial resolution.

Raman Spectroscopy. In this work, we have used the optical characterization tool, where Raman spectroscopy can be done with other kinds of spectroscopy. Here, Nd:YAG (532 nm) with low optical power (5 mW) is used to excite the material. After the excitation of the sample, the scattered light that comprises the Raman, Rayleigh scattered light, and reflected laser line is collected by 20× objective with a NA = 0.45 and directed toward the spectrometer. Gratings with groove densities from 300 to 1800 grooves/mm can be selected according to our requirement of spectral resolutions and spectrum range. After the spectrometer, we detect the dispersed spectrum onto the thermoelectrically cooled charge-coupled device (CCD). We used a long-pass filter, which blocks the laser line and filters out unwanted strong signals. As the excitation laser is not focused, it illuminates different layers of a flake of graphene. To differentiate the emission coming from the different layers of flake, we have narrowed the slit width to collect emission only from a specific position (around 2 um area) of graphene.

Polymer-Assisted Graphene Transfer. Graphene was mechanically exfoliated with scotch tape and then deposited on the SiO_2/Si substrate. These are highly doped Si wafers with ∼300 nm SiO_2 on top and are common substrates on which graphene is optically visible.[52,53] Prior to the transfer, the wafers were rinsed in acetone (15 s) and isopropanol (10 s) and then cleaned in plasma asher three times for 60 s each under 5 mbar pressure of monoatomic oxygen. This process is known to produce larger graphene flakes.[54] After identification of graphene on the substrate using optical microscopy and Raman spectroscopy, the sample was spin-coated with a polymer (cellulose acetate butyrate (CAB) mixed with ethyl acetate with the proportion 1 g/4 mL CAB/EA) and then heated up to ∼80 °C for 6 min. Because the coated film is transparent, graphene can always be located under an optical microscope. A ∼2 mm × 2 mm CAB area containing graphene is then selected and cut. Because the polymer is hydrophobic, it lifts (together with the graphene flake) upon adding a drop of water. The cut film is then transferred to the InAs substrate using a tweezer. Once the film is placed in the desired position, the sample is heated up to ∼150 °C for 10−15 min. During this step, water desorbs and the CAB polymer as well as the graphene flake will stick better onto the new substrate. The polymer residuals are then removed by keeping the sample in acetone overnight and rinsing in isopropanol afterward for 5 min. Upon dissolving the polymer, the

https://doi.org/10.1021/acsanm.2c03891
ACS Appl. Nano Mater. 2022, 5, 17919−17927

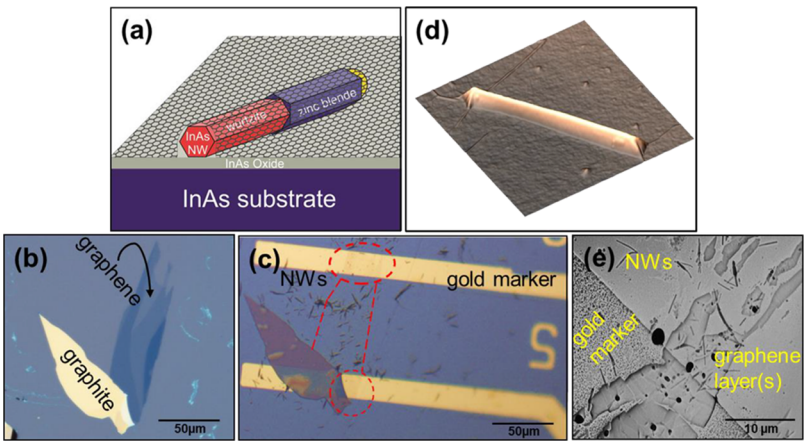

Figure 1. Schematics of the experiments and microscopy images of the samples. (a) Schematic representation of the sample structure. Graphene is folding over an InAs NW placed on an InAs substrate. The oxides present at the interface are subsequently removed by atomic hydrogen treatment. For details on NW morphology, see Figure S1. (b) Graphite and graphene flakes are identified on SiO_2/Si by optical microscopy. The specific thicknesses in terms of monolayer, bilayer, and more can be obtained using the contrast on SiO_2/Si and Raman measurements[45] (Figure S4) prior to the transfer to the final InAs substrate. Here, the very bright blue region is single-layer graphene. The darker the blue, the thicker the layer. The thick graphite flake in vicinity of graphene layer(s) appears as light yellow. (c) Magnified optical microscopy image showing gold markers (yellow bars) and a graphite flake in the vicinity of graphene (for a bigger overview see Figure S3). While graphene is invisible on InAs substrate, it can be seen on gold markers (red dashed lines). (d) 3D AFM image of a NW covered with graphene. (e) LEEM image showing graphene, NWs, and gold markers clearly. (c) and (e) are not recorded on the same samples.

position of the transferred graphene layers can be checked with optical microscope again[55] (Figure S2).

RESULTS AND DISCUSSION

The results of the transfer of graphene onto an InAs substrate with previously deposited InAs NWs are shown in Figure 1. To allow easy navigation on the sample and investigate suitability for future device incorporation, optical lithography is used. Au patterns are thus created on the InAs(111)B substrates prior to NW deposition and graphene transfer (Figure S3). InAs NWs are deposited onto the sample from the original growth substrate using a dry deposition method.[56] To transfer the graphene, we use the well-established polymer-assisted technique;[48] more details are found in the Methods and Materials section. Single/multilayer graphene is initially identified on a SiO_2/Si wafer (highly doped Si wafers with ∼300 nm SiO_2 on top) before transferring (Figure 1b), and its thickness is estimated considering its color contrast under an optical microscope and confirmed using Raman spectroscopy[45] (Figure S4). The graphene is then transferred using polymer embedding (Figure S2) as described in the Methods and Materials section. A single-layer graphene on InAs is not visible in the optical microscope; thus, to ensure identification, we use a part connected to many layers of graphene (graphite) as seen in Figure 1b,c. The presence of graphene on InAs NWs and the substrate is verified by AFM (Figures 1d and 2) and LEEM (Figure 1e). In AFM, graphene is identified both by the difference in contrast and by observation of the height difference between the flake and the surrounding InAs. LEEM is highly surface sensitive, and single and multilayer graphene can be clearly distinguished both on the InAs and the Au markers. This confirms the presence and the integrity of the graphene as well as the presence of NWs under and next to the graphene. The same microscope is used later for XPEEM and μXPS studies, which is performed on the same area of the sample after each treatment.

AFM was used to investigate the graphene/graphite folding over the NWs as seen in Figures 1d and 2. The graphene-covered areas are clearly distinguishable in AFM, and specific areas of the sample as seen in optical microscopy images can be identified. Using AFM, it is possible to estimate how closely the single/bilayer or multilayer graphene folds around them (Figure S5). During AFM measurements, ∼20 nanowires could be investigated with various degrees of graphene coverage. As the diameter observed in the AFM is a convolution of the shape of the tip and the NW, it is useful to also study wires half covered with graphene layer(s) as this allows a direct comparison of the shape change induced by the graphene using the same tip. The location of specific graphene flakes and specific areas with wires under these flakes was possible using the optical microscopy images as maps. Partially covered InAs NWs were located in the AFM and imaged as shown in Figure 2a,b for single/bilayer and multilayer graphene, respectively. The thickness of the layers can be estimated from the AFM images as well as seen in Figure 2c,d. From these profiles, it is seen that the single/bilayer graphene conforms very well around the NW (Figure 2c) when comparing profiles of the wire with/without graphene. For a more detailed analysis, the NW geometry (as described in the SI (see Figure S1)) must be considered. The NWs have two hexagonal segments, one with wurtzite (Wz) crystal structure (∼1 μm long) and another with zincblende (Zb) crystal structure (∼0.8 μm long). Depending on the orientation of the NW on the substrate, this will then lead to different thickness profiles as viewed from the top by the AFM (as discussed in Section 1 of the SI). Two cases are possible: (1) if the side facet of the Wz segment is parallel to the substrate surface, the wire width will appear almost similar along the whole wire, while the height will differ substantially, and (2) if the Zb segment is parallel to the substrate surface, the wire diameter will appear significantly different for the two segments. Even though the absolute width of the NWs as observed by the AFM is a convolution of the tip and the NW profiles, a relative change of the diameter of the wire should be visible down to ∼1 nm (AFM resolution). This is seen in Figure S6 for a NW in orientation (2) where the diameter difference between the

https://doi.org/10.1021/acsanm.2c03891
ACS Appl. Nano Mater. 2022, 5, 17919−17927

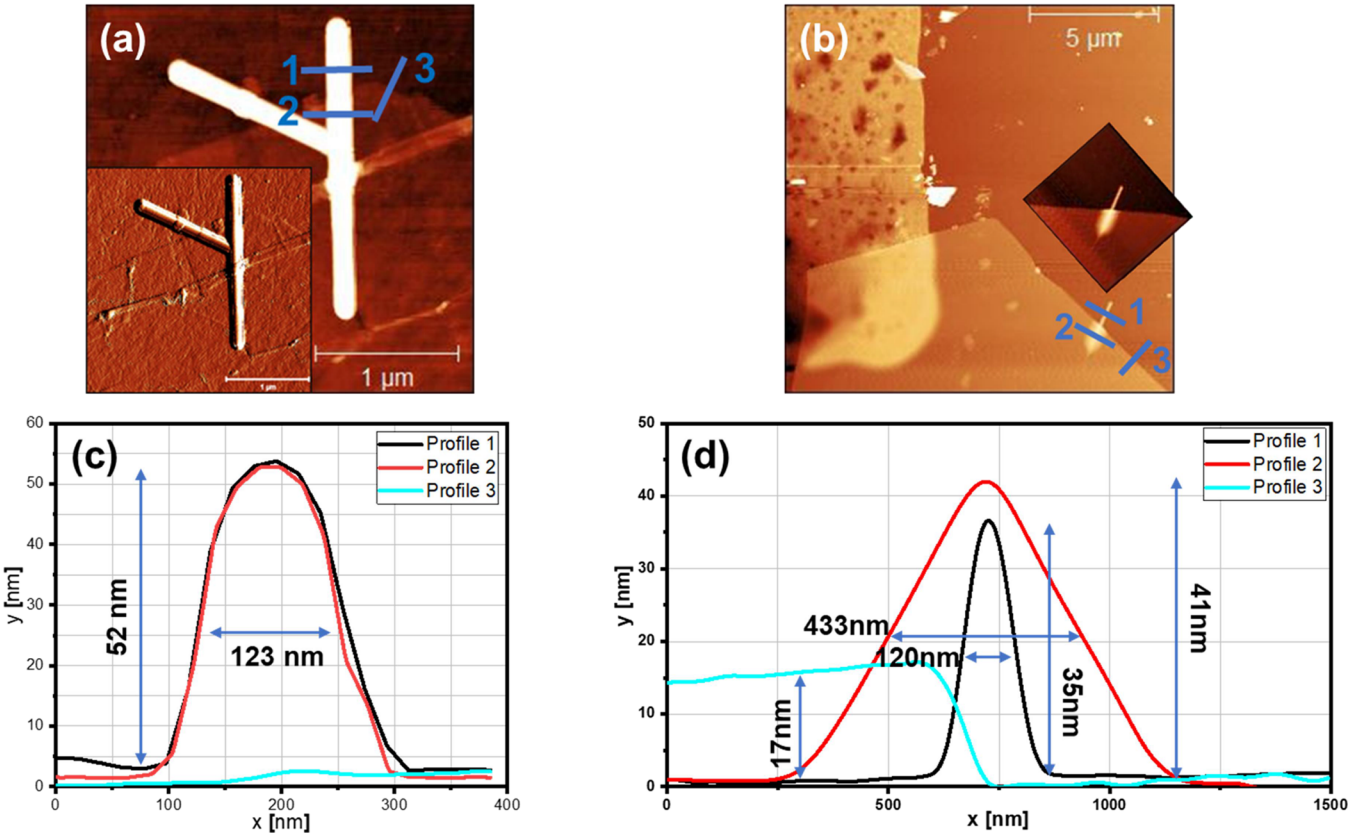

Figure 2. AFM on NWs covered with graphene/graphite. (a) Two NWs partially covered under graphene. Inset: error mode AFM image showing the folding mechanism of graphene over NWs in more details. (b) NW partially covered with thick graphite flake. The graphite flake has covered both the gold markers (thick, porous object at the top left corner of the image) and InAs substrate. Inset: magnified AFM image showing the folding of graphite over the NW. (c) Comparison between uncovered NW (profile 1) and NW covered with graphene (profile 2) (the graphene boundary on the InAs substrate is shown with profile 3, cyan color). The difference between profiles 1 and 2 is negligible, indicating the tight folding of the single/bilayer graphene covering over the NW. (d) Width comparison between covered and uncovered parts of the NW under thick graphite (the distance between the layer and substrate is approximately 17 nm at their border as extracted from profile 3). Note that the height of profile 2 has been offset to the lowest point aligned with profile 1 for easy width comparison between the two profiles. In the original image, it is positioned 17 nm above the substrate (in line with the multilayer graphene). As can be seen, despite the thickness of the covering multilayer graphene, it folds over the NW. However, the width difference between covered and uncovered parts of the NW is significant.

two crystal parts of the NW (as seen from the top) is significant and interestingly can be distinguished even under several layers of graphene. This shows the ability of even a few layers of graphene to conform to the varying shape of the underlying NW. In Figure 2, we find that the NW is oriented on the surface such that the projection does not show a significant observable variation in the width (orientation 1, discussed above). Focusing on the area close to the boundary between the graphene-covered and uncovered parts of the wire and line profiles, which were measured across the NW (profiles 1 and 2 in Figure 2c), are identical (within the precision of the AFM). This indicates that the single/bilayer graphene folds to ∼1 nm of the NW. These two profiles are measured on the same segment of the NW (estimated from the known position of the crystal segment boundary), which makes the comparison simple. Profiles measured further along the NW of Figure 2a inside the graphene-covered area show a smaller height and similar width as those from the uncovered part, which is consistent with the tight folding of the graphene around the NW, when taking the shape of the wire into account. For the multilayer case (Figure 2d), a height of 17 nm corresponding to 50 layers of graphene (layer separation of 0.35 nm) is found. This thick layer folds much more broadly over the wire falling off with a linear slope with a decline of 3°. The difference is attributed to the higher stiffness of the multilayer film.

A key point is to achieve chemical control of the interface between the graphene and the semiconductor surface. While the interface should be mostly free from residues of the polymer (used in the transfer), there will be a native oxide on the InAs and potentially water or OH groups.[27] To remove the native oxide and other impurities, annealing in atomic hydrogen has been efficient for the surfaces of InAs substrates and NWs.[40,41] Following a similar procedure as in refs 40, 41, samples are cleaned using atomic hydrogen at 400 °C at a pressure of 5×10^{-6} mbar for 25 min (for more information about hydrogen cleaning, see the Methods and Materials section).

Before proceeding with the chemical analysis, we briefly investigate the influence of annealing on the graphene folding over the NWs. A direct comparison has been performed on NWs covered with graphene before and after hydrogen cleaning (Figures S6 and S7) using AFM. It should be noted that since the sample is removed from ultra-high vacuum (UHV) after hydrogen cleaning to perform AFM, the InAs can re-oxidize. The lateral shape of the graphene layers on the substrate is similar before and after cleaning. The shallow holes observed in the free InAs areas are known to appear on such

https://doi.org/10.1021/acsanm.2c03891
ACS Appl. Nano Mater. 2022, 5, 17919−17927

surfaces after hydrogen cleaning.[57] The line profile analysis performed across the NWs before and after hydrogen cleaning shows that after the cleaning, the multilayer graphene appears to conform more tightly around the NW, reducing the full width at half maximum (FWHM) to the values close to the bare wire FWHMs (Figures S6d and S7d) by ∼20 nm when comparing the same wire and the same position on the wire. The step heights between the substrate and the graphene are reported to vary from 0.4 up to 3 nm.[58−60] This distance can be modified for instance by annealing the sample (above 100 °C) or by changing the humidity of the environment.[61,62] In the present case, annealing in atomic hydrogen reduces the distance between the graphene and the III−V substrate from typically about 1.2−0.55 nm (Figures S6e and S7e). Similar profile comparisons that show the same phenomenon have been performed at different locations on the sample. Another example is presented in Figures S6f,g and S7f,g. This indicates that annealing the sample during the hydrogen cleaning causes the graphene to conform tighter over the substrate and NWs.

Next, we investigate the ability of atomic hydrogen to remove native oxides in the graphene-III−V interface while maintaining the sample morphology. Graphene, Au markers, and NWs were identified using LEEM as seen in Figures 1e and S8a, and the same area could then be identified in XPEEM. During the synchrotron-based measurements, a similar number of nanowires as in the AFM studies were imaged. PEEM imaging of secondary electrons (Sec-PEEM) recorded before and after hydrogen cleaning are compared in Figure 3a,b (for overview see SI, Figure S8b). The image

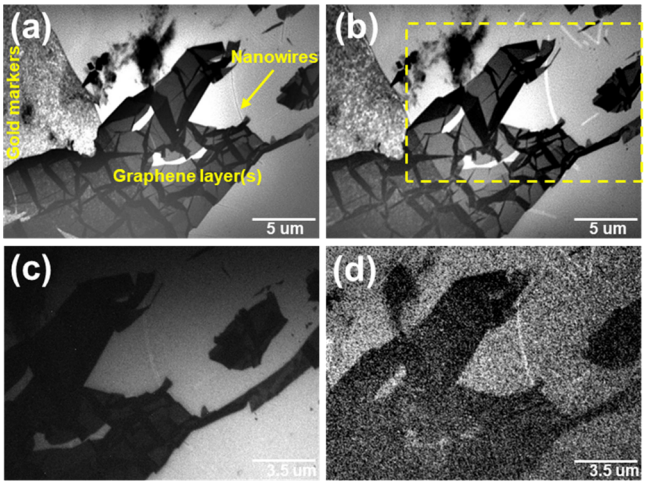

Figure 3. Morphological and elemental analysis of the samples. (a) Sec-PEEM image recorded at a photon energy of 100 eV. The graphene (single and folded double layer), Au markers, and NWs are visible as indicated. The image is recorded prior to atomic hydrogen cleaning. (b) Sec-PEEM image recorded after hydrogen cleaning. (c) XPEEM In 4d core-level map recorded approximately in the area marked with a yellow dashed line in (b) before hydrogen cleaning. (d) XPEEM In 4d core-level map recorded in the same area after hydrogen cleaning.

contrast by secondary electrons will depend on work function and doping of the material and gives a strong contrast between areas with different graphene thicknesses and different materials on the surface. As a result, the morphology and potential changes are clearly seen in Sec-PEEM. It is found that the morphology does not change before and after hydrogen cleaning, indicating that the graphene, Au pattern, and NWs are structurally intact. XPEEM maps were recorded to probe the structural and elemental/chemical composition of the graphene/InAs interfaces. In 4d core-level XPEEM images were recorded with an energy window of $\Delta E \sim 0.5$ eV. These images will give In element mapping across the sample area illuminated by the photon beam (20 μm × 20 μm). As can be seen by comparing Figure 3a,c, the areas containing graphene and the Au markers appear dark, while the InAs regions are brighter in the In 4d images of Figure 3c. This is reasonable as the low mean free path of electrons at the chosen photon energy will result in both the Au and even the single-layer graphene attenuating the photoelectron signal from the In underneath. After the cleaning (Figure 3d), one can still see the same pattern of brighter and darker areas as before and there is no indication of In droplet formation, which can occur on the InAs surface.[63] The difference in contrast between the two In 4d images is due to the chemical shift of the In 4d peak as the oxide is removed; this alters which part of the In peak is effectively imaged (as the images are recorded with the same kinetic energy of the electrons), but in both cases the In is observed.

More quantitative spectroscopic chemical information was extracted by recording μXPS of relevant core levels from various regions of interest (ROIs). We have extracted the signal from two different ROIs, one area covered by graphene and one without. The spectra have been fitted using the IGOR Pro software, assuming Voigt line shapes.[64] Details about the fitting process and parameters can be found in the SI.

As 3d core-level spectra for areas covered and uncovered by graphene, both before and after atomic hydrogen treatment, are shown in Figure 4. Four doublet components are needed to successfully fit the spectra of the un-annealed sample (Figure

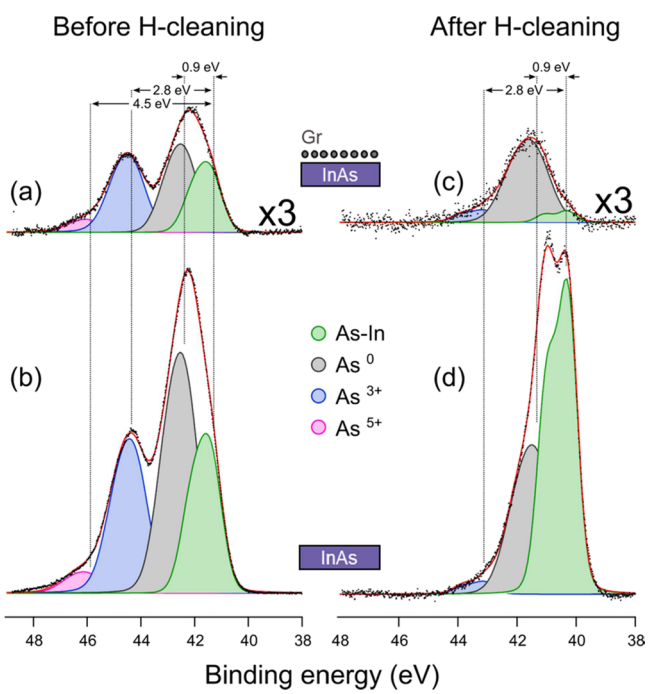

Figure 4. XP spectra of the As 3d core level obtained from the areas identified in the PEEM images as covered and uncovered by graphene. (a) Covered area before H-cleaning. (b) Uncovered area before H-cleaning. (c) Covered area after H-cleaning. (d) Uncovered area after H-cleaning.

https://doi.org/10.1021/acsanm.2c03891
ACS Appl. Nano Mater. 2022, 5, 17919−17927

4a,b). The peak at lowest binding energy (green) corresponds to As in the bulk (As−In). The two components at 2.8 (blue) and 4.5 eV (pink) higher binding energy can be attributed to the As^{3+} and As^{5+} states of the native oxide as in As_2O_3 and As_2O_5, respectively, in agreement with the literature.[57−67] The remaining peak, at a binding energy of 0.9 eV above that of the bulk component, can be attributed to As^0, as it occurs in metallic As, As antisites, or other As defects.[68] It should be noted that the same components can be found both on the graphene-covered and uncovered areas, while the absolute intensity of the As 3d signal is lower in the covered area, due to the attenuation by the graphene layer.

After the cleaning procedure (Figure 4c,d), the As^{5+} component of the native oxide has completely disappeared and the As^{3+} peak has been reduced to levels close to the detection limit. The reduction has occurred on the areas both with and without graphene. This is an important result as it has previously been found[46] that hydrogen treatments underneath graphene can be hindered up to 800 °C. On the graphene-free area, the As^0 component is also reduced and the bulk As component increased after hydrogen treatment, while on the graphene-covered area, the As^0 component become dominating. We assume this discrepancy to be due to excess As atoms after the hydrogen treatment at elevated temperatures, which can desorb from the uncovered InAs surface, while metallic As remains at the surface if it is covered by graphene.

For a more complete picture of the oxide removal, we also monitored the In 4d core levels. The untreated sample (Figure 5a,b), both in graphene-covered and uncovered areas, is dominated by a broad feature. This feature can be fitted by two doublets (shown in blue and green) which are attributed to In-oxide and bulk In−As, respectively.[67] The chemical shift between both components is ∼0.7 eV, which according to the literature[65,66] indicates a mixture of both In^{1+} and In^{3+} oxide components, as in In_2O and In_2O_3.

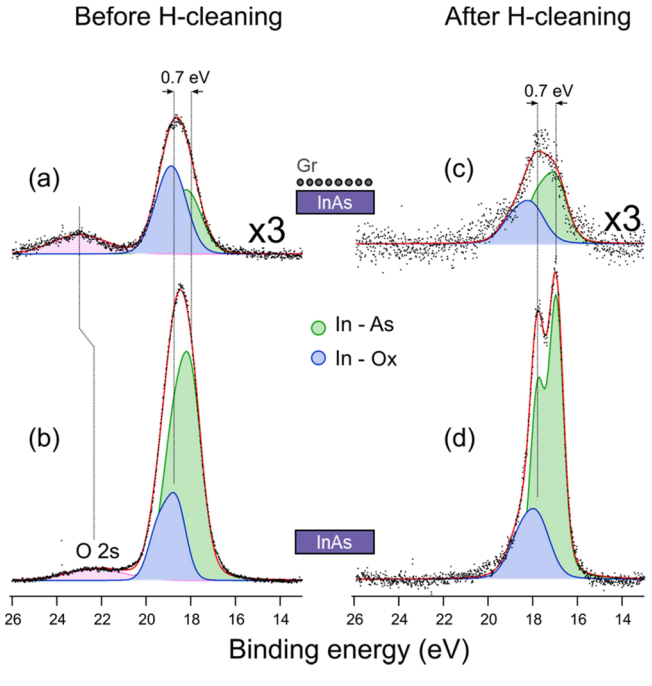

Figure 5. In 4d core-level spectra for areas covered/uncovered by graphene. (a) Covered area before H-cleaning. (b) Uncovered area before H-cleaning. (c) Covered area after H-cleaning. (d) Uncovered area after H-cleaning.

The peak at ca. 23 eV is attributed to the O 2s core level, which is not detectable after the cleaning treatment, in line with the effective oxide removal seen in the As core-level spectra.

After hydrogen treatment, the amount of In-oxide has been reduced in the graphene-free area (Figure 5d) and to an even larger extent in the graphene-covered area (Figure 5c). This confirms that the graphene does not prevent oxide removal from the underlying substrate. However, the cleaning is less effective for In-oxides than it is for Ax-oxides. This is due to In-oxides being energetically more stable than As-oxides,[69] and therefore residues of In-oxides can be left even after hydrogen treatment, as observed experimentally in previous studies.[66,68,70,71]

The XPS results further confirm the quality of the graphene after cleaning. C 1s spectra (Figure S9) recorded from the graphene area look exactly the same before and after the cleaning, dominated by the sp^2 component,[72,73] which we interpret as a sign that the graphene is not dissolved or degraded by the cleaning process and stays intact. In addition, to further investigate the intactness of graphene layer(s) upon hydrogen treatment, Raman characterization of graphene layer(s) on the original deposition substrate before and after hydrogen treatment was performed. The results in Figure S10 show that Raman signal does not change after the hydrogen treatment, which is another indication that removal of oxides by atomic hydrogen annealing will leave the graphene intact.

From the XPS analysis, we can therefore conclude that the H-cleaning has reduced most of the oxides on both graphene-covered and uncovered areas, with some residues of mainly In-oxides left on both areas, characterized by minor stoichiometry differences. We do not observe substantial degradation of the graphene during the process.

CONCLUSIONS

In conclusion, we found that using atomic hydrogen, it is possible to reduce the InAs native oxide underneath graphene. Few/single-layer graphene is found to fold tightly around InAs NWs, and both the NWs and graphene are intact after the cleaning procedure with the graphene folding more tightly around the NWs. The conclusions are based on a wide range of microscopic techniques. For a number of photovoltaic applications that utilize graphene in conjunction with a semiconductor,[26] interface control is crucial to avoid carrier scattering on defects or trapping in defect states. In particular, the removal of surface oxides at relatively low temperature (which can be achieved with atomic hydrogen annealing) improves contact properties and improves performance of both optoelectronic and quantum technology relevant devices.[32−35] Thus, effective oxide removal and cleaning procedures open for improved efficiency of such devices. This would also be important for NW solar cells in which the surface plays a significant role in determining the efficiency of the device[74] where graphene can act as a transparent electrode. Doubling of mobility has also recently been attributed to atomic hydrogen annealing, in NW devices for scalable quantum and optoelectronics.[31] Finally, the tight folding properties of the graphene and the clean interface would open up interesting prospects for using graphene as a wrap-around gate electrode for quantum technologies.[24] A large contact area is needed to achieve low resistance in the contacts, and well-defined

https://doi.org/10.1021/acsanm.2c03891
ACS Appl. Nano Mater. 2022, 5, 17919−17927

electrical fields inside the NW depend on both tight and well-defined folding as well as the removal of oxide related defects that can charge and screen. The present demonstration of interface control is thus a step toward realizing such applications. As interface control even with atomic hydrogen beneath graphene is untrivial due to the rather untransparent nature of the material, which in some cases have hindered interface reaction. Finally, the hydrogen treatment for removal of the native oxide has been proven to work for a wide range of semiconductor materials, indicating that the present conclusions are not limited to InAs but extends more widely.

■ ASSOCIATED CONTENT

Supporting Information

The Supporting Information is available free of charge at https://pubs.acs.org/doi/10.1021/acsanm.2c03891.

The nanowire geometry, polymer-assisted graphene transfer, overview of the samples, Raman spectroscopy, measuring the distance between graphene layer(s) and substrate, comparison—before and after hydrogen cleaning, LEEM, XPEEM, Sec-PEEM, and XPS complementary results (PDF)

■ AUTHOR INFORMATION

Corresponding Author

Anders Mikkelsen − *Department of Physics and NanoLund, Lund University, 22100 Lund, Sweden;* orcid.org/0000-0002-9761-0440; Email: anders.mikkelsen@sljus.lu.se

Authors

S. Fatemeh Mousavi − *Department of Physics and NanoLund, Lund University, 22100 Lund, Sweden;* orcid.org/0000-0003-1455-4437

Yen-Po Liu − *Department of Physics and NanoLund, Lund University, 22100 Lund, Sweden;* orcid.org/0000-0003-0144-0991

Giulio D'Acunto − *Department of Physics and NanoLund, Lund University, 22100 Lund, Sweden;* orcid.org/0000-0002-0564-6906

Andrea Troian − *Max IV Laboratory, Lund University, 22100 Lund, Sweden*

José M. Caridad − *Department of Physics and NanoLund, Lund University, 22100 Lund, Sweden; Department of Applied Physics and USAL NanoLab, University of Salamanca, 37008 Salamanca, Spain;* orcid.org/0000-0001-8943-1170

Yuran Niu − *Max IV Laboratory, Lund University, 22100 Lund, Sweden*

Lin Zhu − *Max IV Laboratory, Lund University, 22100 Lund, Sweden*

Asmita Jash − *Department of Physics and NanoLund, Lund University, 22100 Lund, Sweden*

Vidar Flodgren − *Department of Physics and NanoLund, Lund University, 22100 Lund, Sweden*

Sebastian Lehmann − *Department of Physics and NanoLund, Lund University, 22100 Lund, Sweden;* orcid.org/0000-0002-4091-905X

Kimberly A. Dick − *NanoLund, Lund University, 22100 Lund, Sweden; Centre for Analysis and Synthesis, Lund University, 22100 Lund, Sweden*

Alexei Zakharov − *Max IV Laboratory, Lund University, 22100 Lund, Sweden;* orcid.org/0000-0002-1269-6813

Rainer Timm − *Department of Physics and NanoLund, Lund University, 22100 Lund, Sweden;* orcid.org/0000-0001-8914-5924

Complete contact information is available at: https://pubs.acs.org/10.1021/acsanm.2c03891

Author Contributions

The manuscript was written through contributions of all authors. All authors have given approval to the final version of the manuscript.

Notes

The authors declare no competing financial interest.

■ ACKNOWLEDGMENTS

This work was supported by the Swedish Research Council (VR) and the Swedish Foundation for Strategic Research (SSF). We acknowledge MAX IV Laboratory for experiments performed at the MAXPEEM beamline under proposal [20200397]. Research conducted at MAX IV, a Swedish national user facility, is supported by the Swedish Research Council under contract 2018-07152 and 2014-04580, the Swedish Governmental Agency for Innovation Systems under contract 2018-04969, and Formas under contract 2019-02496.

■ ABBREVIATIONS

NW, nano wires
LEEM, low-energy electron microscopy
XPEEM, X-ray photoemission electron microscopy
Sec-PEEM, secondary photoemission electron microscopy
XPS, X-ray photoelectron spectroscopy

■ REFERENCES

(1) Kim, Y.; Cruz, S. S.; Lee, K.; Alawode, B. O.; Choi, C.; Song, Y.; Johnson, J. M.; Heidelberger, C.; Kong, W.; Choi, S.; Qiao, K.; Almansouri, I.; Fitzgerald, E. A.; Kong, J.; Kolpak, A. M.; Hwang, J.; Kim, J. Remote Epitaxy through Graphene Enables Two-Dimensional Material-Based Layer Transfer. *Nature* **2017**, *544*, 340−343.

(2) Bolotin, K. I.; Sikes, K. J.; Jiang, Z.; Klima, M.; Fudenberg, G.; Hone, J.; Kim, P.; Stormer, H. L. Ultrahigh Electron Mobility in Suspended Graphene. *Solid State Commun.* **2008**, *146*, 351−355.

(3) Castro Neto, A. H.; Guinea, F.; Peres, N. M. R.; Novoselov, K. S.; Geim, A. K. The Electronic Properties of Graphene. *Rev. Mod. Phys.* **2009**, *81*, 109−162.

(4) Das Sarma, S.; Adam, S.; Hwang, E. H.; Rossi, E. Electronic Transport in Two-Dimensional Graphene. *Rev. Mod. Phys.* **2011**, *83*, 407−470.

(5) Li, H.; Li, S.; Naik, M. H.; Xie, J.; Li, X.; Wang, J.; Regan, E.; Wang, D.; Zhao, W.; Zhao, S.; Kahn, S.; Yumigeta, K.; Blei, M.; Taniguchi, T.; Watanabe, K.; Tongay, S.; Zettl, A.; Louie, S. G.; Wang, F.; Crommie, M. F. Imaging Moiré Flat Bands in Three-Dimensional Reconstructed WSe_2/WS_2 Superlattices. *Nat. Mater.* **2021**, *20*, 945−950.

(6) Majumder, K.; Barshilia, D.; Majee, S. Study on Graphene Based Next Generation Flexible Photodetector for Optical Communication. *Graphene* **2018**, *07*, 9−16.

(7) Liu, W.; Jackson, B. L.; Zhu, J.; Miao, C.-Q.; Chung, C.-H.; Park, Y.-J.; Sun, K.; Woo, J.; Xie, Y.-H. Large Scale Pattern Graphene Electrode for High Performance in Transparent Organic Single Crystal Field-Effect Transistors. *ACS Nano* **2010**, *4*, 3927−3932.

(8) Bong, J.; Han, J.; Lee, J.; Kim, S.; Ju, S. Fabrication of Highly Transparent Nanowire Transistors with One-Step-Processed Graphene Gate−Source−Drain Electrodes. *Appl. Phys. Express* **2013**, *6*, No. 055103.

(9) Li, X.; Sun, T.; Zhou, K.; Hong, X.; Tang, X.; Wei, D.; Feng, W.; Shen, J.; Wei, D. Broadband InSb/Si Heterojunction Photodetector

with Graphene Transparent Electrode. *Nanotechnology* **2020**, *31*, 315204.
(10) Stöberl, U.; Wurstbauer, U.; Wegscheider, W.; Weiss, D.; Eroms, J. Morphology and Flexibility of Graphene and Few-Layer Graphene on Various Substrates. *Appl. Phys. Lett.* **2008**, *93*, No. 051906.
(11) Wang, X.; Wu, P. Highly Thermally Conductive Fluorinated Graphene Films with Superior Electrical Insulation and Mechanical Flexibility. *ACS Appl. Mater. Interfaces* **2019**, *11*, 21946−21954.
(12) Wei, N.; Xu, L.; Wang, H.-Q.; Zheng, J.-C. Strain Engineering of Thermal Conductivity in Graphene Sheets and Nanoribbons: A Demonstration of Magic Flexibility. *Nanotechnology* **2011**, *22*, No. 105705.
(13) Yelgel, C.; Srivastava, G. P.; Miwa, R. H. *Ab Initio* Investigation of the Electronic Properties of Graphene on InAs(111)A. *J. Phys.: Condens. Matter* **2012**, *24*, No. 485004.
(14) Al Balushi, Z. Y.; Wang, K.; Ghosh, R. K.; Vilá, R. A.; Eichfeld, S. M.; Caldwell, J. D.; Qin, X.; Lin, Y.-C.; DeSario, P. A.; Stone, G.; Subramanian, S.; Paul, D. F.; Wallace, R. M.; Datta, S.; Redwing, J. M.; Robinson, J. A. Two-Dimensional Gallium Nitride Realized via Graphene Encapsulation. *Nat. Mater.* **2016**, *15*, 1166−1171.
(15) Al Balushi, Z. Y.; Miyagi, T.; Lin, Y.-C.; Wang, K.; Calderin, L.; Bhimanapati, G.; Redwing, J. M.; Robinson, J. A. The Impact of Graphene Properties on GaN and AlN Nucleation. *Surf. Sci.* **2015**, *634*, 81−88.
(16) Wong-Leung, J.; Yang, I.; Li, Z.; Karuturi, S. K.; Fu, L.; Tan, H. H.; Jagadish, C. Engineering III−V Semiconductor Nanowires for Device Applications. *Adv. Mater.* **2020**, *32*, No. 1904359.
(17) Barrigón, E.; Heurlin, M.; Bi, Z.; Monemar, B.; Samuelson, L. Synthesis and Applications of III−V Nanowires. *Chem. Rev.* **2019**, *119*, 9170−9220.
(18) Wallentin, J.; Anttu, N.; Asoli, D.; Huffman, M.; Åberg, I.; Magnusson, M. H.; Siefer, G.; Fuss-Kailuweit, P.; Dimroth, F.; Witzigmann, B.; Xu, H. Q.; Samuelson, L.; Deppert, K.; Borgström, M. T. InP Nanowire Array Solar Cells Achieving 13.8% Efficiency by Exceeding the Ray Optics Limit. *Science* **2013**, *339*, 1057−1060.
(19) Luo, Y.; Yan, X.; Zhang, J.; Li, B.; Wu, Y.; Lu, Q.; Jin, C.; Zhang, X.; Ren, X. A Graphene/Single GaAs Nanowire Schottky Junction Photovoltaic Device. *Nanoscale* **2018**, *10*, 9212−9217.
(20) Mukherjee, A.; Yun, H.; Shin, D. H.; Nam, J.; Munshi, A. M.; Dheeraj, D. L.; Fimland, B.-O.; Weman, H.; Kim, K. S.; Lee, S. W.; Kim, D.-C. Single GaAs Nanowire/Graphene Hybrid Devices Fabricated by a Position-Controlled Microtransfer and an Imprinting Technique for an Embedded Structure. *ACS Appl. Mater. Interfaces* **2019**, *11*, 13514−13522.
(21) Liao, L.; Lin, Y.-C.; Bao, M.; Cheng, R.; Bai, J.; Liu, Y.; Qu, Y.; Wang, K. L.; Huang, Y.; Duan, X. High-Speed Graphene Transistors with a Self-Aligned Nanowire Gate. *Nature* **2010**, *467*, 305−308.
(22) Miao, J.; Hu, W.; Guo, N.; Lu, Z.; Liu, X.; Liao, L.; Chen, P.; Jiang, T.; Wu, S.; Ho, J. C.; Wang, L.; Chen, X.; Lu, W. High-Responsivity Graphene/InAs Nanowire Heterojunction Near-Infrared Photodetectors with Distinct Photocurrent On/Off Ratios. *Small* **2015**, *11*, 936−942.
(23) Teng, D.; Wang, K.; Li, Z. Graphene-Coated Nanowire Waveguides and Their Applications. *Nanomaterials* **2020**, *10*, 229.
(24) Kim, M.-W.; Park, S.-W.; Park, K.-T.; Min, B.-J.; Ku, J.-H.; Ko, J.-Y.; Choi, J. S.; No, Y.-S. All-Graphene-Contact Electrically Pumped On-Demand Transferrable Nanowire Source. *Nano Lett.* **2022**, *22*, 1316−1323.
(25) Kanne, T.; Marnauza, M.; Olsteins, D.; Carrad, D. J.; Sestoft, J. E.; de Bruijckere, J.; Zeng, L.; Johnson, E.; Olsson, E.; Grove-Rasmussen, K.; Nygård, J. Epitaxial Pb on InAs Nanowires for Quantum Devices. *Nat. Nanotechnol.* **2021**, *16*, 776−781.
(26) Behura, S. K.; Wang, C.; Wen, Y.; Berry, V. Graphene−Semiconductor Heterojunction Sheds Light on Emerging Photovoltaics. *Nat. Photonics* **2019**, *13*, 312−318.
(27) Pirkle, A.; Chan, J.; Venugopal, A.; Hinojos, D.; Magnuson, C. W.; McDonnell, S.; Colombo, L.; Vogel, E. M.; Ruoff, R. S.; Wallace, R. M. The Effect of Chemical Residues on the Physical and Electrical Properties of Chemical Vapor Deposited Graphene Transferred to SiO_2. *Appl. Phys. Lett.* **2011**, *99*, 122108.
(28) Chan, J.; Venugopal, A.; Pirkle, A.; McDonnell, S.; Hinojos, D.; Magnuson, C. W.; Ruoff, R. S.; Colombo, L.; Wallace, R. M.; Vogel, E. M. Reducing Extrinsic Performance-Limiting Factors in Graphene Grown by Chemical Vapor Deposition. *ACS Nano* **2012**, *6*, 3224−3229.
(29) Chen, H.; Zhang, X.-L.; Zhang, Y.-Y.; Wang, D.; Bao, D.-L.; Que, Y.; Xiao, W.; Du, S.; Ouyang, M.; Pantelides, S. T.; Gao, H.-J. Atomically Precise, Custom-Design Origami Graphene Nanostructures. *Science* **2019**, *365*, 1036−1040.
(30) Wu, Y.; Zhai, D.; Pan, C.; Cheng, B.; Taniguchi, T.; Watanabe, K.; Sandler, N.; Bockrath, M. Quantum Wires and Waveguides Formed in Graphene by Strain. *Nano Lett.* **2018**, *18*, 64−69.
(31) Beznasyuk, D. V.; Martí-Sánchez, S.; Kang, J.-H.; Tanta, R.; Rajpalke, M.; Stankevič, T.; Christensen, A. W.; Spadaro, M. C.; Bergamaschini, R.; Maka, N. N.; Petersen, C. E. N.; Carrad, D. J.; Jespersen, T. S.; Arbiol, J.; Krogstrup, P. Doubling the Mobility of InAs/InGaAs Selective Area Grown Nanowires. *Phys. Rev. Mater.* **2022**, *6*, No. 034602.
(32) Webb, J. L.; Knutsson, J.; Hjort, M.; Gorji Ghalamestani, S.; Dick, K. A.; Timm, R.; Mikkelsen, A. Electrical and Surface Properties of InAs/InSb Nanowires Cleaned by Atomic Hydrogen. *Nano Lett.* **2015**, *15*, 4865−4875.
(33) Alexander-Webber, J. A.; Groschner, C. K.; Sagade, A. A.; Tainter, G.; Gonzalez-Zalba, M. F.; Di Pietro, R.; Wong-Leung, J.; Tan, H. H.; Jagadish, C.; Hofmann, S.; Joyce, H. J. Engineering the Photoresponse of InAs Nanowires. *ACS Appl. Mater. Interfaces* **2017**, *9*, 43993−44000.
(34) Li, Z.; Tan, H. H.; Jagadish, C.; Fu, L. III−V Semiconductor Single Nanowire Solar Cells: A Review. *Adv. Mater. Technol.* **2018**, *3*, No. 1800005.
(35) Sourribes, M. J. L.; Isakov, I.; Panfilova, M.; Warburton, P. A. Minimization of the Contact Resistance between InAs Nanowires and Metallic Contacts. *Nanotechnology* **2013**, *24*, No. 045703.
(36) Hjort, M.; Wallentin, J.; Timm, R.; Zakharov, A. A.; Håkanson, U.; Andersen, J. N.; Lundgren, E.; Samuelson, L.; Borgström, M. T.; Mikkelsen, A. Surface Chemistry, Structure, and Electronic Properties from Microns to the Atomic Scale of Axially Doped Semiconductor Nanowires. *ACS Nano* **2012**, *6*, 9679−9689.
(37) Timm, R.; Mikkelsen, A. Surface Functionalization of III−V Nanowires. In *Fundamental Properties of Semiconductor Nanowires*; Fukata, N.; Rurali, R., Eds.; Springer: Singapore, 2021; pp 111−141.
(38) Bell, G. R.; Kaijaks, N. S.; Dixon, R. J.; McConville, C. F. Atomic Hydrogen Cleaning of Polar III−V Semiconductor Surfaces. *Surf. Sci.* **1998**, *401*, 125−137.
(39) Badawy, G.; Zhang, B.; Rauch, T.; Momand, J.; Koelling, S.; Jung, J.; Gazibegovic, S.; Moutanabbir, O.; Kooi, B. J.; Botti, S.; Verheijen, M. A.; Frolov, S. M.; Bakkers, E. P. A. M. Electronic Structure and Epitaxy of CdTe Shells on InSb Nanowires. *Adv. Sci.* **2022**, *9*, No. 2105722.
(40) Knutsson, J. V.; Lehmann, S.; Hjort, M.; Lundgren, E.; Dick, K. A.; Timm, R.; Mikkelsen, A. Electronic Structure Changes Due to Crystal Phase Switching at the Atomic Scale Limit. *ACS Nano* **2017**, *11*, 10519−10528.
(41) Hjort, M.; Knutsson, J. V.; Mandl, B.; Deppert, K.; Lundgren, E.; Timm, R.; Mikkelsen, A. Surface Morphology of Au-Free Grown Nanowires after Native Oxide Removal. *Nanoscale* **2015**, *7*, 9998−10004.
(42) Wang, M.; Cai, L.; Wang, Y.; Zhou, F.; Xu, K.; Tao, X.; Chai, Y. Graphene-Draped Semiconductors for Enhanced Photocorrosion Resistance and Photocatalytic Properties. *J. Am. Chem. Soc.* **2017**, *139*, 4144−4151.
(43) Morrow, W. K.; Pearton, S. J.; Ren, F. Review of Graphene as a Solid State Diffusion Barrier. *Small* **2016**, *12*, 120−134.
(44) Scardamaglia, M.; Struzzi, C.; Zakharov, A.; Reckinger, N.; Zeller, P.; Amati, M.; Gregoratti, L. Highlighting the Dynamics of Graphene Protection toward the Oxidation of Copper Under

https://doi.org/10.1021/acsanm.2c03891
ACS Appl. Nano Mater. 2022, 5, 17919−17927

Operando Conditions. *ACS Appl. Mater. Interfaces* **2019**, *11*, 29448−29457.
(45) Soman, A.; Burke, R. A.; Li, Q.; Valentin, M. D.; Li, T.; Mao, D.; Dubey, M.; Gu, T. Hydrogen Plasma Exposure of Monolayer MoS_2 Field-Effect Transistors and Prevention of Desulfurization by Monolayer Graphene. *ACS Appl. Mater. Interfaces* **2020**, *12*, 37305−37312.
(46) Guisinger, N. P.; Rutter, G. M.; Crain, J. N.; First, P. N.; Stroscio, J. A. Exposure of Epitaxial Graphene on SiC(0001) to Atomic Hydrogen. *Nano Lett.* **2009**, *9*, 1462−1466.
(47) Hjort, M.; Kratzer, P.; Lehmann, S.; Patel, S. J.; Dick, K. A.; Palmstrøm, C. J.; Timm, R.; Mikkelsen, A. Crystal Structure Induced Preferential Surface Alloying of Sb on Wurtzite/Zinc Blende GaAs Nanowires. *Nano Lett.* **2017**, *17*, 3634−3640.
(48) McKibbin, S. R.; Colvin, J.; Troian, A.; Knutsson, J. V.; Webb, J. L.; Otnes, G.; Dirscherl, K.; Sezen, H.; Amati, M.; Gregoratti, L.; Borgström, M. T.; Mikkelsen, A.; Timm, R. Operando Surface Characterization of InP Nanowire p−n Junctions. *Nano Lett.* **2020**, *20*, 887−895.
(49) Hjort, M. *III-V Nanowire Surfaces*; Lunds Universitet, 2016.
(50) Magnusson, M. H.; Deppert, K.; Malm, J.-O.; Bovin, J.-O.; Samuelson, L. Size-Selected Gold Nanoparticles by Aerosol Technology. *Nanostruct. Mater.* **1999**, *12*, 45−48.
(51) Wagner, R. S.; Ellis, W. C. Vapor-liquid-solid mechanism of single crystal growth. *Appl. Phys. Lett.* **1964**, *4*, 89−90.
(52) Ni, Z. H.; Wang, H. M.; Kasim, J.; Fan, H. M.; Yu, T.; Wu, Y. H.; Feng, Y. P.; Shen, Z. X. Graphene Thickness Determination Using Reflection and Contrast Spectroscopy. *Nano Lett.* **2007**, *7*, 2758−2763.
(53) Caridad, J. M.; Rossella, F.; Bellani, V.; Grandi, M. S.; Diez, E. Automated Detection and Characterization of Graphene and Few-Layer Graphite via Raman Spectroscopy: Automated Detection and Characterization of Graphene and FLG. *J. Raman Spectrosc.* **2011**, *42*, 286−293.
(54) Huang, Y.; Sutter, E.; Shi, N. N.; Zheng, J.; Yang, T.; Englund, D.; Gao, H.-J.; Sutter, P. Reliable Exfoliation of Large-Area High-Quality Flakes of Graphene and Other Two-Dimensional Materials. *ACS Nano* **2015**, *9*, 10612−10620.
(55) Caridad, J. M.; Power, S. R.; Lotz, M. R.; Shylau, A. A.; Thomsen, J. D.; Gammelgaard, L.; Booth, T. J.; Jauho, A.-P.; Bøggild, P. Conductance Quantization Suppression in the Quantum Hall Regime. *Nat. Commun.* **2018**, *9*, 659.
(56) Hjort, M.; Lehmann, S.; Knutsson, J.; Timm, R.; Jacobsson, D.; Lundgren, E.; Dick, K. A.; Mikkelsen, A. Direct Imaging of Atomic Scale Structure and Electronic Properties of GaAs Wurtzite and Zinc Blende Nanowire Surfaces. *Nano Lett.* **2013**, *13*, 4492−4498.
(57) Hilner, E.; Lundgren, E.; Mikkelsen, A. Surface Structure and Morphology of InAs(111)B with/without Gold Nanoparticles Annealed under Arsenic or Atomic Hydrogen Flux. *Surf. Sci.* **2010**, *604*, 354−360.
(58) Caridad, J. M.; Rossella, F.; Bellani, V.; Maicas, M.; Patrini, M.; Díez, E. Effects of Particle Contamination and Substrate Interaction on the Raman Response of Unintentionally Doped Graphene. *J. Appl. Phys.* **2010**, *108*, No. 084321.
(59) Novoselov, K. S.; Geim, A. K.; Morozov, S. V.; Jiang, D.; Zhang, Y.; Dubonos, S. V.; Grigorieva, I. V.; Firsov, A. A. Electric Field Effect in Atomically Thin Carbon Films. *Science* **2004**, *306*, 666−669.
(60) Roscher, S.; Hoffmann, R.; Ambacher, O. Determination of the Graphene−Graphite Ratio of Graphene Powder by Raman 2D Band Symmetry Analysis. *Anal. Methods* **2019**, *11*, 1224−1228.
(61) Lee, H.; Park, J. Y. Height Determination of Single-Layer Graphene on Mica at Controlled Humidity Using Atomic Force Microscopy. *Rev. Sci. Instrum.* **2019**, *90*, 103702.
(62) Gammelgaard, L.; Caridad, J. M.; Cagliani, A.; Mackenzie, D. M. A.; Petersen, D. H.; Booth, T. J.; Bøggild, P. Graphene Transport Properties upon Exposure to PMMA Processing and Heat Treatments. *2D Mater.* **2014**, *1*, No. 035005.
(63) Mandl, B.; Stangl, J.; Hilner, E.; Zakharov, A. A.; Hillerich, K.; Dey, A. W.; Samuelson, L.; Bauer, G.; Deppert, K.; Mikkelsen, A. Growth Mechanism of Self-Catalyzed Group III−V Nanowires. *Nano Lett.* **2010**, *10*, 4443−4449.
(64) Schmid, M.; Steinrück, H.-P.; Gottfried, J. M. A New Asymmetric Pseudo-Voigt Function for More Efficient Fitting of XPS Lines: New Asymmetric Pseudo-Voigt Function for Efficient XPS Line Fitting. *Surf. Interface Anal.* **2014**, *46*, 505−511.
(65) Timm, R.; Fian, A.; Hjort, M.; Thelander, C.; Lind, E.; Andersen, J. N.; Wernersson, L.-E.; Mikkelsen, A. Reduction of Native Oxides on InAs by Atomic Layer Deposited Al_2O_3 and HfO_2. *Appl. Phys. Lett.* **2010**, *97*, 132904.
(66) D'Acunto, G.; Troian, A.; Kokkonen, E.; Rehman, F.; Liu, Y.-P.; Yngman, S.; Yong, Z.; McKibbin, S. R.; Gallo, T.; Lind, E.; Schnadt, J.; Timm, R. Atomic Layer Deposition of Hafnium Oxide on InAs: Insight from Time-Resolved *In Situ* Studies. *ACS Appl. Electron. Mater.* **2020**, *2*, 3915−3922.
(67) Brennan, B.; Hughes, G. Identification and Thermal Stability of the Native Oxides on InGaAs Using Synchrotron Radiation Based Photoemission. *J. Appl. Phys.* **2010**, *108*, No. 053516.
(68) D'Acunto, G.; Kokkonen, E.; Shayesteh, P.; Boix, V.; Rehman, F.; Mosahebfard, Z.; Lind, E.; Schnadt, J.; Timm, R. Oxygen Relocation during HfO_2 ALD on InAs. *Faraday Discuss.* **2022**, *236*, 71.
(69) Hollinger, G.; Skheyta-Kabbani, R.; Gendry, M. Oxides on GaAs and InAs Surfaces: An x-Ray-Photoelectron-Spectroscopy Study of Reference Compounds and Thin Oxide Layers. *Phys. Rev. B* **1994**, *49*, 11159−11167.
(70) Troian, A.; Knutsson, J. V.; McKibbin, S. R.; Yngman, S.; Babadi, A. S.; Wernersson, L.-E.; Mikkelsen, A.; Timm, R. InAs-Oxide Interface Composition and Stability upon Thermal Oxidation and High-k Atomic Layer Deposition. *AIP Adv.* **2018**, *8*, 125227.
(71) Timm, R.; Head, A. R.; Yngman, S.; Knutsson, J. V.; Hjort, M.; McKibbin, S. R.; Troian, A.; Persson, O.; Urpelainen, S.; Knudsen, J.; Schnadt, J.; Mikkelsen, A. Self-Cleaning and Surface Chemical Reactions during Hafnium Dioxide Atomic Layer Deposition on Indium Arsenide. *Nat. Commun.* **2018**, *9*, 1412.
(72) Kovtun, A.; Jones, D.; Dell'Elce, S.; Treossi, E.; Liscio, A.; Palermo, V. Accurate Chemical Analysis of Oxygenated Graphene-Based Materials Using X-Ray Photoelectron Spectroscopy. *Carbon* **2019**, *143*, 268−275.
(73) Siokou, A.; Ravani, F.; Karakalos, S.; Frank, O.; Kalbac, M.; Galiotis, C. Surface Refinement and Electronic Properties of Graphene Layers Grown on Copper Substrate: An XPS, UPS and EELS Study. *Appl. Surf. Sci.* **2011**, *257*, 9785−9790.
(74) Barrigón, E.; Zhang, Y.; Hrachowina, L.; Otnes, G.; Borgström, M. T. Unravelling Processing Issues of Nanowire-Based Solar Cell Arrays by Use of Electron Beam Induced Current Measurements. *Nano Energy* **2020**, *71*, No. 104575.

https://doi.org/10.1021/acsanm.2c03891
ACS Appl. Nano Mater. 2022, 5, 17919−17927